Atomistic study of nanotwins in NiTi shape memory alloys

Yuan Zhong, Ken Gall, and Ting Zhu[a)]
Woodruff School of Mechanical Engineering, Georgia Institute of Technology, Atlanta, Georgia 30332, USA

(Received 4 April 2011; accepted 24 June 2011; published online 11 August 2011)

Atomistic simulations are performed to study the structure and geometrical limit of nanoscale twins in NiTi shape memory alloys. We analyze compound twins as narrow as ~1 nm, involving a few atomic layers. A novel nanotwinned structure is found, forming through the martensitic transformation of sublattices. We predict the temperatures of phase transformation, which are consistent with experimental measurements. The results provide an atomistic basis for further study of nanometer length scale effects on the martensitic phase transformation and shape memory behavior. © *2011 American Institute of Physics*. [doi:10.1063/1.3621429]

I. INTRODUCTION

The generation of large and reversible strains in shape memory alloys is governed by the diffusionless martensitic phase transformation of a crystal lattice in response to applied thermomechanical loadings.[1–5] Recent development in the processing, characterization, and nanomechanical testing of nanostructured shape memory alloys provides opportunities of revealing the nanometer length scale effects on martensitic phase transformation, and may offer practical solutions of efficient shape memory, actuation, and mechanical damping in microscale and nanoscale devices.[6–21]

Understanding the martensitic transformation in nanostructured shape memory alloys is predicated upon knowing the structures of various phases. However, due to the structural complexity at the nanometer scale, it is nontrivial to generate their atomic configurations for further study. To this end, here we combine the crystallographic theory and atomistic simulation to study the nanotwinned structure and phase transformation. We utilize the crystallographic theory of twinned martensite[22,23] to construct the initial twin structures. Then the atomistic calculation is performed by using an empirical interatomic potential,[24] which has been benchmarked by experimental values and first principles calculations. Our atomistic simulation goes beyond the crystallographic theory by providing more structural details and mechanistic insights at the sublattice level. Compared to the first principles calculation,[25–32] it enables an efficient exploration of twinned microstructures, and can be further utilized to study their spatial-temporal evolution and associated phenomena of plasticity and fracture at the atomic scale. Considering the complexity of martensite microstructures, as well as a large range of time and length scales involved in the martensitic transformation processes, the empirical potential-based atomistic modeling approach developed is expected to play an important role in bridging experiments, continuum models,[33–44] and *ab initio* calculations for understanding the transformation mechanisms in shape memory alloys.

This work is focused on understanding the atomic-scale twin structures in NiTi shape memory alloys, and is motivated by recent high resolution transmission electron microcopy (HRTEM) imaging of nanocrystalline NiTi, showing the unique martensitic phase of nanoscale compound twins spanning the entire nanosized grain.[26] It is useful to recall that a typical martensitic phase transition in NiTi involves the transformation from a high temperature B2 cubic austenite phase to a low temperature B19′ monoclinic martensitic phase.[5] The most characteristic feature of martensitic transformation is the formation of twins, where the arrangement of the lattice on one side of the twin boundary plane is a mirror reflection of those on the other. Twin martensites are conventionally classified as type I (i.e., the twin plane is a rational crystal plane), type II (i.e., the twin shear is a rational crystallographic direction), and compound twin (both the twin plane and twin shear are rational); their rigorous definitions can be found, e.g., in the review by Christian and Mahajan.[2] In coarse-grained NiTi, type I and type II twins are more often observed than compound twins. This can be rationalized in terms of the requirement of deformation compatibility at extended interfaces (i.e., habit planes) between martensite and austenite. Namely, compared to the compound twins, the formation of type I and type II twins can better achieve geometrical compatibility with the parent B2 phase of austenite.[45] In contrast, compound twins often form in nanocrystalline NiTi.[26] Further, the twin-related variants can span the entire nanosized grain, so that the kinematic incompatibility caused by martensitic transformation is accommodated by the grain boundary rather than the habit plane. Such a size effect of nanostructures on martensitic phase transformation has been studied by Waitz and co-workers by considering the competing effects of twin boundary, grain boundary, and elastic energies associated with the twin variants and the surrounding matrix.[26,42] However, it is not yet well understood regarding the atomic basis of why they form and how stable they are.

In this paper, we study the atomic-level details of nanotwinned structures by combining the crystallographic theory and atomistic simulation. We analyze the compound twins as narrow as ~1 nm, involving a few atomic layers. The HRTEM images of twinned structures[26] provide the validation for our simulations. We discover a novel transformation mode that may have implications for the martensitic phase transition of materials with the complex lattice structure, common to crystalline alloys and compounds. We also study temperature-driven phase transformations and the size effects. The results

[a)]Electronic mail: ting.zhu@me.gatech.edu.

provide an atomistic structural basis for further investigation of martensitic phase transformation and shape memory behavior of the shape memory alloys at the nanometer scale.[46]

II. METHODS

A. Interatomic potential

A many-body interatomic potential is used to describe the NiTi system. This potential was originally developed by Lai and Liu,[24] but is improved in this work with a smooth cutoff behavior to avoid the diverging forces in simulations involving large atomic displacements. As a Finnis–Sinclair-type potential,[47] the potential function is constructed by using the second-moment approximation of the tight-binding theory. The total energy of the system is expressed as

$$E = \sum_i \left\{ \sum_{j \neq i} A_{\alpha\beta} \exp\left[-p_{\alpha\beta} \left(\frac{r_{ij}}{d_{\alpha\beta}} - 1 \right) \right] - \sqrt{\sum_{j \neq i} F(r_{ij})} \right\}, \tag{1}$$

where

$$F(r_{ij}) = \xi_{\alpha\beta}^2 \exp\left[-2q_{\alpha\beta} \left(\frac{r_{ij}}{d_{\alpha\beta}} - 1 \right) \right]. \tag{2}$$

TABLE I. Potential parameters for NiTi.

	Ni–Ni	Ti–Ti	Ni–Ti or Ti–Ni
D (Å)	2.49	2.95	2.607
A (eV)	0.104	0.153	0.3
P	11.198	9.253	7.9
ξ (eV)	1.591	1.879	2.48
Q	2.413	2.513	3.002
c_3	27.3341	122.395	47.851 3
c_2	−7.54308	−34.205	−12.923 62
c_1	−0.26286	−1.005 4	−0.572 708
c_0	0.13561	0.590 12	0.248 676

Here, r_{ij} is the distance between atom i and j, and α and β denote the type of atoms (Ni or Ti) at sites i and j, respectively. In Eq. (1), the first term in the curly bracket describes the pair interaction and the second term represents the many-body effect. The potential parameters were fitted to the properties of the B2 phase at 0 K from first principles calculations, and the potential cutoff radius r_c was determined to be 4.2 Å.[24] However, $F(r_{ij})$ in Eq. (2) and its derivative about r_{ij} are nonzero at r_c. To be suitable for use in molecular statics and dynamics simulations that generally require smooth energies and interatomic forces, we have modified the potential by changing $F(r_{ij})$ in Eq. (2) as follows,

$$F(r_{ij}) = \begin{cases} \xi_{\alpha\beta}^2 \exp\left[-2q_{\alpha\beta} \left(\frac{r_{ij}}{d_{\alpha\beta}} - 1 \right) \right], & r_{ij} \leq r_1 \\ c_{3,\alpha\beta}(r_{ij} - r_1)^3 + c_{2,\alpha\beta}(r_{ij} - r_1)^2 + c_{1,\alpha\beta}(r_{ij} - r_1) + c_{0,\alpha\beta}, & r_1 < r_{ij} \leq r_c \end{cases}. \tag{3}$$

In Eq. (3), for given r_1 the four coefficients of $c_{0,\alpha\beta}$ to $c_{3,\alpha\beta}$ are solely determined by four continuity conditions, namely, $F(r_{ij})$ and its first derivative are continuous at both r_1 and r_c. We determine r_1 by optimizing the predicted properties.

The potential parameters are listed in Table I with $r_1 = 4.0$ Å and $r_c = 4.2$ Å. This modified potential not only removes the discontinuities at r_c, but also improves the predicted properties, including the lattice constant and energy of various phases of NiTi, as compared with *ab initio* calculations in Table II. In our atomistic calculations of single phases, both the atomic coordinates, as well as the side lengths and angles of the simulation box are fully relaxed by using the stress-controlled conjugate gradient energy minimization.[48,49]

B. Crystallographic theory of twinned martensite

We have utilized the crystallographic theory of twinned martensite to facilitate the atomistic simulation of nanotwins in NiTi. Although it is desirable to generate and analyze the nanotwins by direct molecular dynamics (MD) simulations, the attainable twin structures are limited because of the well-known time scale limitation of MD and the associated low efficiency of sampling the atomistic energy landscape when the atomic-level structure is not precisely known. To overcome these limitations, we construct the initial twin struc-

TABLE II. Comparison of lattice constant, a, b, c, monocline angle β, and the energy per atom E for single phases and compound twins, as well as their differences with the energy of the B2 phase E_{B2}. Results from this work are indicated by the Finnis–Sinclair (FS) potential. The experimental and *ab initio* values are taken from Knowles and Smith (Ref. 50) and Wagner and Windl (Ref. 32), respectively. The last two rows list the properties of nanotwins with monolayers of monoclinic unit cells, shown in Figs. 6(b) and 6(c), respectively.

	Structure	a (Å)	b (Å)	c (Å)	β(deg)	E (eV)	$E - E_{B2}$ (eV)
B2	Experiment	3.015	4.264	4.264	90		
	FS-potential	3.008	4.253	4.253	90	−5.022	
	Ab initio	3.008	4.253	4.253	90		
BCO	FS-potential	2.994	4.001	4.883	107.86	−5.069	−0.047
	Ab initio	2.953	3.993	4.951	108.52		−0.050
B19′	Experiment	2.889	4.120	4.622	96.8		
	FS-potential	3.005	4.022	4.466	98.08	−5.073	−0.051
	Ab initio	2.941	4.035	4.685	97.78		−0.044
B19′	Twin[a]	3.062	4.018	4.391	Ti 94.44 Ni 93.96	−5.058	−0.036
B19′	Twin[b]	3.011	4.022	4.464	98.43	−5.075	−0.053
		3.011	4.022	4.416	90		

[a]Figure 6(b).
[b]Figure 6(c).

tures based on the crystallographic theory of twinned martensite, and then relax the system by using the stress-controlled conjugate gradient energy minimization. In this way, various type I, type II, and compound twins can be accessed for detailed analyses. Moreover, the direct atomistic simulation can go beyond the crystallographic theory to reveal more sublattice level information and insights.

The crystallographic theory of twinned martensite requires an input of the transformation matrix from the cubic parent phase to the martensitic phase. With this information, the twinning elements, including the twin plane normal and twin shear, can be predicted by solving the twinning equation that governs the kinematic compatibility between adjoining twin variants. Consider, as an example, the martensitic transformation from the B2 to B19′ phase. Following the notation used by Knowles and Smith,[50] the transformation takes a tetragonal unit cell of the parent B2 phase (Fig. 1) into a monoclinic cell of the product B19′ phase. The associated lattice deformation involves a uniform expansion or contraction of the tetragonal cell, followed by a simple shear. In the orthonormal basis $(\mathbf{i}', \mathbf{j}', \mathbf{k}')$ given in Fig. 1, the deformation gradient matrix can be represented by

$$\mathbf{F} = \frac{1}{a_0}\begin{bmatrix} b/\sqrt{2} & 0 & 0 \\ 0 & c\sin\beta/\sqrt{2} & 0 \\ 0 & -c\cos\beta/\sqrt{2} & a \end{bmatrix}, \tag{4}$$

where a_0 is the lattice parameter of the cubic unit cell in B2, a, b, c are the lattice parameters of the monoclinic unit cell in B19′, and β is the associated monoclinic angle between the edges with lengths of a and c. Prior to martensitic transformation, $a = a_0$, $b = c = \sqrt{2}a_0$, and $\beta = 90°$. The shuffling of atoms in the cell was ignored in the crystallographic theory of martensitic transformation.[50]

Twin variants of the B19′ phase should satisfy the kinematic compatibility condition given by the twinning equation[4]

$$\mathbf{QF}_I - \mathbf{F}_J = \mathbf{m} \otimes \mathbf{n}, \tag{5}$$

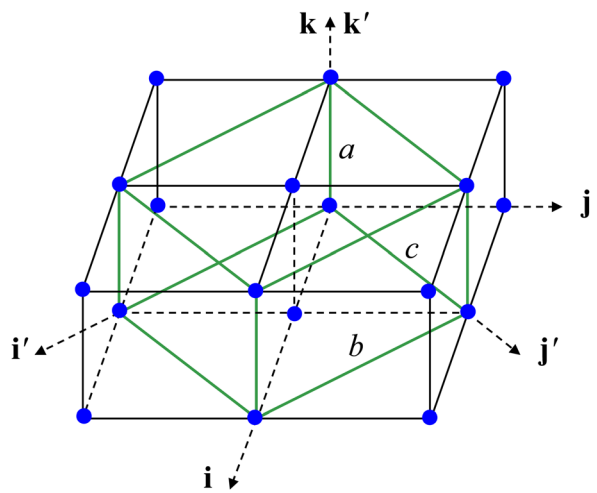

FIG. 1. (Color online) Schematics of a tetragonal unit cell (green lines) and four cubic unit cells (black lines) in the lattice of untransformed B2 parent phase. Only Ni atoms are shown for clarity. The orthonormal vectors $(\mathbf{i}, \mathbf{j}, \mathbf{k})$ are along the cube axes, and the orthonormal vectors $(\mathbf{i}', \mathbf{j}', \mathbf{k}')$ are along the cube directions of $[1\bar{1}0]$, [110], and [001], respectively.

where $\mathbf{F}_I$ and $\mathbf{F}_J$ denote the symmetry-related deformation gradient of variant I and J, respectively, $\mathbf{n}$ is the normal vector of the twinning plane at the untransformed reference B2 state, $\mathbf{m}$ is the twinning shear vector at the transformed current B19′ state, and $[\mathbf{m} \otimes \mathbf{n}]_{ij} = m_i n_j$. Equation (5) essentially requires that any vector lying in the twin plane, which separates the two adjoining variants, should undergo the same deformation when viewed from either side. Note that $\mathbf{Q}$ represents an additional rotation of variant I after the transformation by $\mathbf{F}_I$; namely, the total transformation imposed on variant I is $\mathbf{QF}_I$. The rotation matrix $\mathbf{Q}$ is needed whenever the orientations of the twin plane are different after the transformations of variant I by $\mathbf{F}_I$ and variant J by $\mathbf{F}_J$. For the martensitic transformation from the cubic B2 to monoclinic B19′ phase, there are 12 distinct variants. The transformation is conventionally described in terms of the symmetric deformation matrix $\mathbf{U}$ obtained from the polar decomposition of deformation gradient $\mathbf{F}$. Then there are 132 possible variant pairs between 12 monoclinic variants and those pairs can be classified as type I, type II, or compound twins,[2] as discussed in the introduction. Solutions of Eq. (5) for type I, type II, and compound twins have been cataloged by Hane and Shield.[45] In this work, we focus on compound twins in order to directly compare simulations with available HRTEM images of twinned structures. Detailed solutions of compound twins suitable for atomistic calculations in the periodic supercell, including $\mathbf{F}_I$, $\mathbf{F}_J$, $\mathbf{m}$, and $\mathbf{n}$, are given in the Appendix. Our method is general and applicable to create type I and type II twins, and it can be further developed to produce complex twin microstructures (e.g., twinned wedges in the austenite matrix[4]) for providing an atomistic structural basis of studying their spatial-temporal evolution.

III. RESULTS AND DISCUSSION

A. Single phases

Figure 2 shows the relaxed structures of the B2, B19′, and base-centered orthorhombic (BCO) single phases of equiatomic NiTi. Table II lists the lattice parameter, monoclinic angle and energy per atom for each phase calculated by the interatomic potential. Most results given by the potential are close to the available experimental values and *ab*

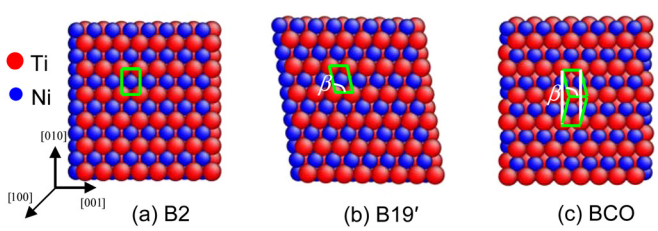

FIG. 2. (Color online) Relaxed atomic structures of single phase, equiatomic NiTi, viewed from the [100] direction in the $(\mathbf{i}', \mathbf{j}', \mathbf{k}')$ basis of Fig. 1. (a) B2 phase, the rectangle indicates a tetragonal unit cell. (b) B19′ phase, the parallelogram indicates a monoclinic unit cell with the monoclinic angle $\beta \approx 98°$. (c) Base-centered orthorhombic (BCO) phases, the rectangle (white lines) indicates a BCO unit cell; the BCO structure can also be considered as a twinned B19′ and each variant consists of one layer of monoclinic unit cell (green lines) with $\beta \approx 107°$.

TABLE III. Elastic constants (GPa) of the B2 phase calculated from the Finnis-Sinclair (FS) potential of this work, in comparison with *ab initio* calculations and experimental measurements at different temperatures.

	FS potential ($T=0$ K)	*Ab initio* ($T=0$ K)	Experimental ($T=298$ K)[a]	Experimental ($T=400$ K)[b]
C_{11}	206.3	183	162	137
C_{12}	135.8	146	129	120
C_{44}	46.9	46	34	34

[a]Reference 52.
[b]Reference 51.

initio calculations. However, the energy of the BCO phase (−5.069 eV/atom) is slightly higher than that of the B19′ phase (−5.073 eV/atom), whereas the more accurate *ab initio* calculations predicted that BCO has a lower energy at zero temperature.[25] On the other hand, the B19′ phase is most commonly observed in experiments at low temperatures.[5] It is still an open question as to the most stable martensitic phase at low temperatures. Nevertheless, the geometric features of nanotwins reported in this work are expected to be robust, as most of them are symmetry related. But one should take caution in interpreting the relative magnitude of energies among various phases and twins predicted by the potential. Also note that as shown in Fig. 2(c), the relaxed BCO phase (with an orthorhombic unit cell in white lines) can be equivalently considered as B19′ twinned at the level of unit cells (green lines) with the resulting monoclinic angle $\beta \approx 107°$. This geometrical view was advanced by Huang *et al.*,[25] providing an interesting connection between nanotwinned and single phase structures. Table III lists the elastic constants of the B2 phase calculated from the interatomic potential at 0 K, which are close to *ab initio* calculations. Due to omission of the temperature effects or lattice vibrations, these results are larger than experimental values measured at and above room temperatures.[51,52]

B. Compound twins

Figures 3 and 4 show the relaxed structures of (001) and (010) compound twins, respectively. Here (001) and (010) refer to the $(\mathbf{i}', \mathbf{j}', \mathbf{k}')$ basis in Fig. 1, and they are equivalent to (001) and (110) in the $(\mathbf{i}, \mathbf{j}, \mathbf{k})$ basis. We focus on a single twin boundary by studying the thick twins, such that neighboring twin boundaries are sufficiently separated to minimize their interactions. The effect of the twin thickness will be addressed later in Fig. 5. Notice that the initial structures of (001) and (010) twins are constructed by using the transformation matrices of Eqs. (A2) and (A1), respectively. When applying these transformation matrices to construct the atomic structures, one can choose to position the mathematical mirror twin plane at various locations, including exactly on an atomic layer or between atomic layers. As a result, several metastable twin-boundary structures are obtained after stress-controlled conjugate gradient energy minimization. The corresponding mirror twin plane is indicated by the dashed line in Figs. 3 and 4. The position of a twin plane is determined according to its definition, i.e., the arrangements of the lattice on one side of the twin boundary plane are mirror reflections of those on the other.

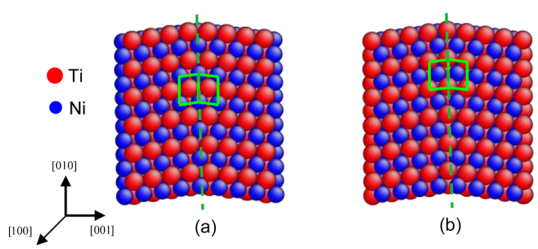

FIG. 3. (Color online) Relaxed structures of (001) compound twins. The mirror twin plane (dashed line) is located on (a) the pure Ni laden layer and (b) the pure Ti layer, respectively.

For the relaxed (001) compound twin shown in Fig. 3, the mirror twin boundary is always located on the atomic plane, irrespective of the position of the twin plane. As the (001) atomic planes consist of alternate pure Ni (small blue atoms) or pure Ti (big red atoms) layers, the mirror twin boundary can be either on a Ni laden plane (Fig. 3(a)) or Ti laden plane (Fig. 3(b)). We define the twin boundary energy, γ, as the excess energy (in reference to the single phase of B19′) divided by the boundary area. The calculated value of γ is, respectively, 0.136 and 0.047 J/m^2, indicating that the twin boundary located on the Ti plane is more energetically favorable than that on the Ni plane.

In contrast, for the relaxed (010) compound twin shown in Fig. 4, the energy minimization results in structures with the twin mirror plane located either on or off the atomic layer. To understand the "on" and "off" possibilities, one should notice the following geometrical feature of (010) planes. In contrast to the (001) planes that involve the alternate pure Ni and pure Ti layers generating the twin structures shown in Fig. 3, the order arrangement of atoms in a (010) plane involves a 2D rectangular net of Ni atoms interpenetrating a rectangular net of Ti atoms. As such, all the (010) planes are equivalent in terms of chemical arrangement of Ni and Ti atoms. Consequently, if the mirror twin plane is located on the atomic layer, there exists only one type of boundary structure, as discussed next with Fig. 4(b). Interestingly, adjacent (010) layers differ by an in-plane shift in the diagonal direction of the 2D rectangle cell of Ni (or Ti) by one-half of the diagonal length. As a result, one period in the [010] direction involves two neighboring (010) atomic planes.

Figure 4(a) shows the relaxed structures when the mirror twin plane is off the atomic layers. One can see that the mirror

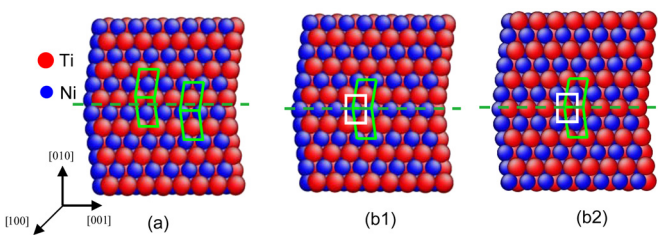

FIG. 4. (Color online) Relaxed structures of (010) compound twins. The mirror twin plane (dashed line) is located (a) off the (010) atomic planes, and (b) on the (010) atomic plane. The front atomic layer in (b1) and (b2) exposes one of the two different (100) atomic planes of the same relaxed structure. The white unit cell of Ti atoms in (b1) and that of Ni in (b2) straddle the twin plane (dashed line), respectively, and remain the rectangular shape.

reflection is only approximately satisfied by unit cells of atoms near the twin boundary. The corresponding twin boundary energy γ is 0.089 J/m^2, larger than 0.014 J/m^2 from the first principles calculation.[26] In contrast, Fig. 4(b) shows the relaxed structure when the mirror twin plane is on the (010) atomic plane. Note that in Figs. 4(b1) and 4(b2) the front atomic layer of the simulation box exposes one of the two different (100) planes of the same relaxed structure, respectively. It is seen that the mirror reflection is obeyed by the parallelogram-shaped unit cells (in green) on the two sides of the twin plane. Moreover, the mirror twin plane is located in the middle of the unit cells in white, and these cells keep the rectangle shape so as to maintain the symmetry about the twin plane. Such boundary is structurally different from that in Fig. 4(a), resulting in a different twin boundary energy $\gamma = -0.0091$ J/m^2. Although the small negative boundary energy could be specific to the interatomic potential, this boundary structure can possibly exist as a metastable state, justified by the local symmetry of the lattice. It follows that this kind of boundary is expected to be observable in experiments, considering that the shape memory alloys generally consist of various co-existing metastable structures. As discussed next, the available HRTEM image[26] shows evidence of their existence.

The HRTEM image of nanocrystalline NiTi by Waitz *et al.* has revealed the formation of nanoscale (010) compound twins that can span the entire grain.[26] It was observed that the thickness of twins varies in the same grain, and the thinnest variant is about 1 nm, involving two layers of monoclinic unit cells. These unit cells seem to be rectangular rather than monoclinic, lending a support to the existence of the boundary structures shown in Fig. 4(b). Systematic HRTEM experiments and *ab initio* calculations are needed to clarify the exact boundary structure.

To understand the effects of the twin thickness, we create (010) compound twins with thicknesses of two, three, and six layers of monoclinic unit cells. Figure 5 shows the cases with the twin mirror plane located between the atomic planes, similar to Fig. 4(a). The twin boundary energies extracted from various twin structures in Fig. 5 are close to $\gamma \approx 0.09$ J/m^2. These nearly constant values indicate the validity of separating the total energy into the bulk and excess interfacial parts for the nanotwinned system. More specifically, for coarse twins, it is common to analyze the optimal twin geometry in terms of competing effects of the increase of the total twin boundary energy with decreasing twin thickness and the associated decrease of the bulk elastic energy caused by the geometric incompatibility of transformed phases with the surrounding materials.[42] The foregoing results show that such an approach can be extended to analyze the nanotwinned structures at low temperatures, considering the nearly constant twin boundary energies at the nanometer scale.

C. Geometrical limit of nanotwins

We have explored the geometrical limit of nanoscale twins with monolayers of the monoclinic unit cell, whereas the hitherto experiment only reveals nanotwins as thin as two layers of monoclinic unit cells in each B19′ variant, as discussed previously. Figure 6 shows the relaxed structures of (010) compound twins with one layer of monoclinic unit cells in each variant. Their boundary structures are similar to those shown in Fig. 4, but the twin thickness is reduced to the minimum. To understand these structures, it is useful to note that the lattice of the B2 phase of NiTi can be viewed as four sets of interpenetrating tetragonal sublattices, as schematically shown in Fig. 6(a). The martensitic transformation from the B2 to B19′ phase can be considered as an expansion or contraction along the edges of the tetragonal unit cell, followed by a simple shear to a monoclinic angle β.

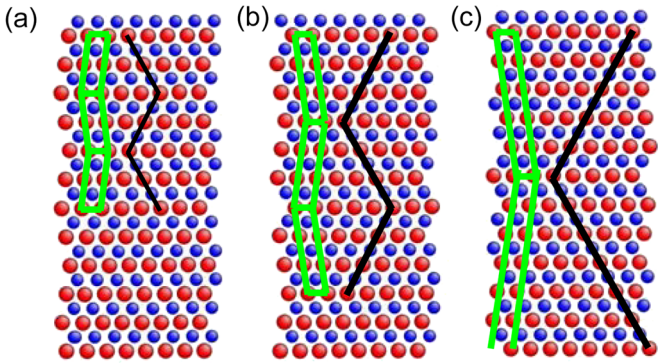

FIG. 5. (Color online) Atomistically simulated twin structures with different twin widths, i.e., each green-colored twin variants comprises (a) two, (b) three, or (c) six layers of monoclinic unit cells. Black lines are drawn for guiding eyes, equivalent to the white lines in the TEM image by Waitz *et al.* (Fig. 2 in Ref. 26).

Figure 6(b) shows the relaxed twin structure when the mirror twin plane is located off the atomic plane, and its twin boundary structure is similar to that in Fig. 4(a). This is a simple case of uniform martensitic transformation, where each of the four sublattices consists of alternate single layer of monoclinic unit cells with $\beta \approx 94°$.

Of particular interest is that a new nanotwinned structure is found: one Ni sublattice and one Ti sublattice undergo martensitic transformations, whereas other Ni and Ti sublattices remain orthorhombic. This mode is discovered from the relaxed structure when the martensitic transformations are imposed according to the matrices in Eq. (A1) with the mirror twin plane positioned at the (010) atomic plane; the relaxed boundary structure is similar to that in Fig. 4(b). Figures 6(c1) and 6(c2) show the same state of such a twinned structure after energy minimization. Notice that because of interpenetration of 3D sublattices, one period in the [100] direction involves two neighboring (100) atomic planes. The front atomic layer of the simulation cell in Figs. 6(c1) and 6(c2) exposes one of the two different (100) planes, respectively. Comparing them with Fig. 6(a), one can see that one sublattice of Ni atoms [green twinned cells in (c1)] and one sublattice of Ti atoms [blue twinned cells in (c2)] consist of variants of single layer of *monoclinic* unit cells ($\beta = 98.43°$), whereas one sublattice of Ti atoms [orange rectangle cells in (c1)] and one sublattice of Ni atoms [pink rectangle cells in (c2)] consist of *orthorhombic* unit cells ($\beta = 90°$). One interesting feature is the tight coupling of sheared and unsheared sublattices, resulting from interpenetration of the multilattices. Although this nanotwinned structure was discovered from

our atomistic simulations of equiatomic NiTi at zero temperature, it is geometrically reasonable and could present as metastable states in other alloy and compound systems with the multilattice structure.[53,54]

The alternate twinned structures shown in Fig. 6 can be considered as a single orthorhombic phase with the period doubled in the twin-plane normal direction of [010]. This geometrical view is motivated by a similar consideration of the single phase BCO as a twinned B19′ with the monoclinic angle $\beta \approx 107°$,[25] as discussed earlier. Of course, there is a notable difference between the two cases: all the sublattices of BCO are equivalent, whereas the new structure involves the interpenetration of alternatively sheared and unsheared sublattices. Moreover, whereas these twin products were obtained by a general procedure of constructing martensites according to Eq. (A1) followed by energy minimization, one may equivalently set up their initial states by shuffling every other (010) atomic plane in the [001] direction—the shuffling method has also been used to study the pathways of martensitic transformation.[28,55]

In the present geometrical limit of monolayer twinned structures, despite the spatial overlap of the bulk and twin boundary regions, the effective twin boundary energy (i.e., the excess energy per unit boundary area in reference to the B19′ monovariant) is still about -0.0089 J/m^2, very close the values of -0.0091 J/m^2 extracted from the previous cases of thicker nanotwins. As explained earlier, one should take caution in interpreting the energy values given by the interatomic potential. However, the geometric features of those nanotwins are symmetry related. They could possibly exist as metastable states, considering that the HRTEM image by Waitz *et al.*[26] has revealed a similar type of thicker nanotwins. Finally, to facilitate the future verification by *ab initio* calculations and experimental measurements, we list in Table II the predicted unit-cell geometry and energy per atom for the monolayer nanotwins shown in Figs. 6(b) and 6(c).

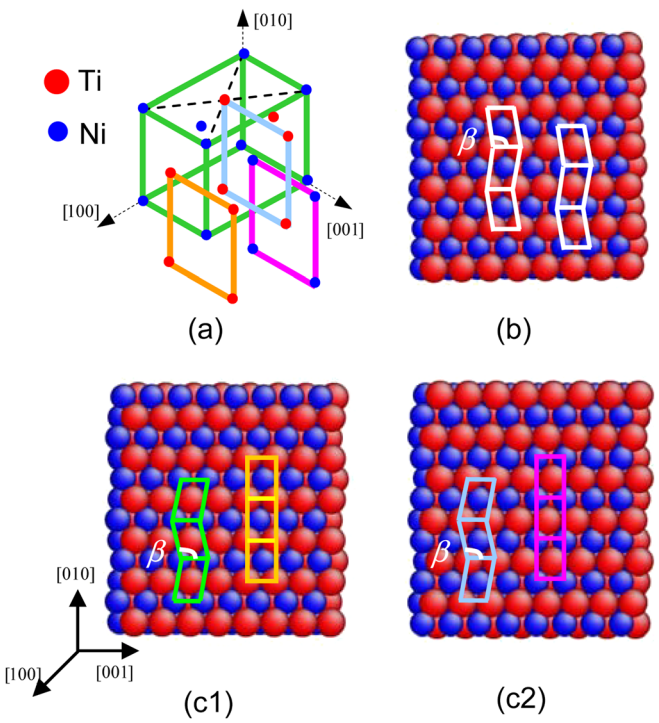

FIG. 6. (Color online) Relaxed atomic structures of (010) twins with the smallest thickness (about 0.5 nm), and each variant consists of one layer of monoclinic unit cells, i.e., two atomic planes. (a) Schematics of four sets of interpenetrating simple orthorhombic sublattices. One Ni sublattice is represented by a 3D green box, and the other Ni sublattice is indicated by a 2D pink rectangle instead of a 3D box for clarity. The two Ti sublattices are indicated by the orange and blue rectangles, respectively. (b) All sublattices are twinned, as indicated by the sheared unit cells. (c) A subset of interpenetrating sublattices is twinned. The front atomic layer of (c1) and (c2) exposes one of the two different (100) atomic planes, respectively. The Ni sublattice in (c1) and Ti sublattice in (c2) are twinned.

D. Phase transformation and size effect

Temperature-driven phase transformation is simulated by using the MD simulation package LAMMPS. We have implemented the NiTi potential in LAMMPS. In MD simulations, the starting structure is monoclinic B19′. The supercell box contains 9216 atoms. The system is subjected to periodic boundary conditions and fully relaxed to zero stresses. The temperature is initially set to 100 K through thermal equilibration. Then the thermal load is applied by linearly varying temperatures in three stages: (I) heating from 100 to 450 K; (II) cooling from 450 to 100 K; (III) reheating until 450 K. The MD simulation of each stage involves 200 000 time steps, each of which is 0.5 fs. The phase transformation is characterized by geometrical changes of the simulation cell in terms of an order parameter, W, defined as the sum of all the shear components of the simulation box. W is further normalized by its maximum value, such that it varies between 0 and 1, corresponding to the cubic B2 and monoclinic B19′ phases, respectively.

Figure 7 shows that in stage I of heating (blue curve), W first increases slightly with temperature due to the effect of thermal expansion. As the temperature is further increased to ~350 K, W decreases sharply to a very small value close to zero. Correspondingly, the B19′ phase, Fig. 7(b), undergoes a structural phase transition to the B2 phase, Fig. 7(c). This indicates that both the start temperature, A_s, and finish temperature, A_f, of the B2 austenite are close to 350 K.

In stage II of cooling (black curve), a similar abrupt change of W is observed as temperature is decreased to ~300 K. This corresponds to the reverse transformation from the B2 austenite to the B19′ martensite. Due to formation of the twinned B19′ structures, Fig. 7(d), W only increases to 0.6, smaller than $W = 1$ of a single B19′ phase. This reduction of W can be attributed to the canceling effect of shearing of adjacent twin variants in the opposite directions, causing a decrease of the overall shear of the simulation box. The corresponding start temperature of the B19′ martensite, M_s, is 310 K and the finish temperature, M_f, is 290 K, indicating that the formation of twinned structures occurs in a relatively narrow temperature range.

In stage III of reheating (red curve), the twinned B19′ structure undergoes the transforms to a single B2 phase. The process starts at ~310 K and finishes at 350 K. Correspondingly, W deceases gradually from 0.6 to 0, in contrast to the abrupt change of W at ~350 K in stage I of heating of a single B19′ phase. Both the decrease of A_s and gradual change of W can be attributed to the presence of twin boundaries

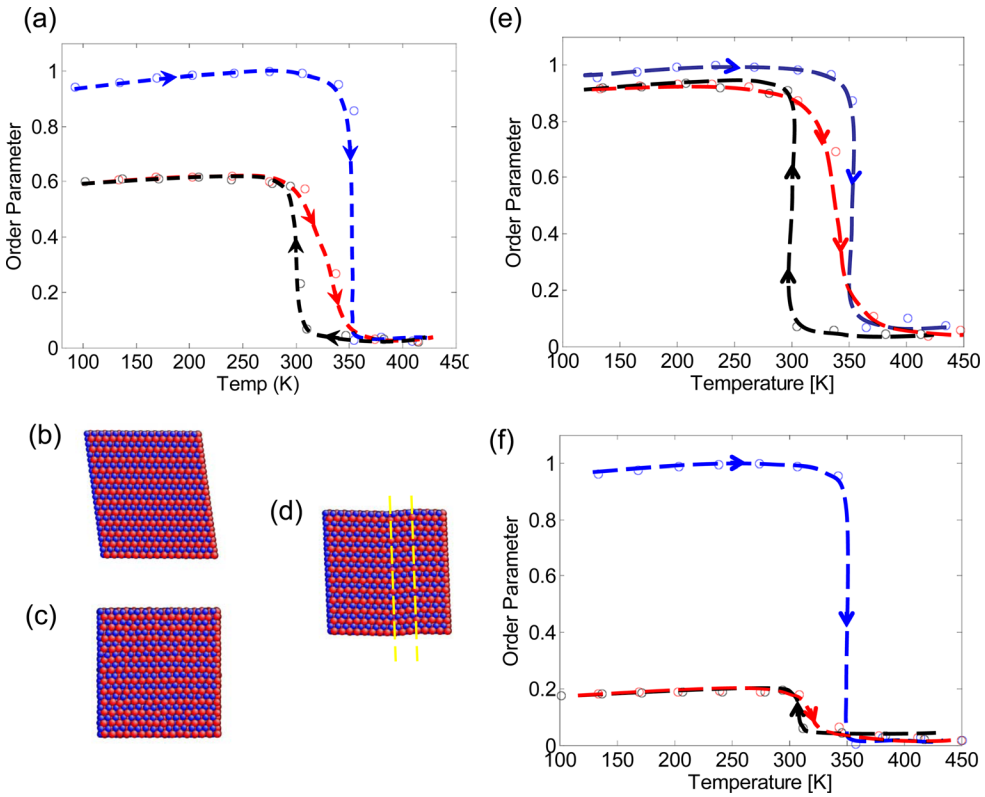

FIG. 7. (Color online) MD simulation of phase transformation for different sizes of the simulation box. (a) The order parameter W as a function of temperature T for three stages of temperature loading: (I) heating (blue), (II) cooling (black), and (III) reheating (red). Symbols represent time-averaged values and lines are drawn to guide eyes. (b) The monoclinic B19′ phase at the beginning of stage I of heating. (c) The cubic B2 phase at the end of stage I of heating. (d) The B19′ phase at the end of stage II of cooling, forming nanotwins indicated by dashed lines. (e) Same as (a) except that the volume is 1/8 of that in (a). (f) Same as (a) except that the volume is 8 times of that in (a).

acting as the heterogeneous interfaces to facilitate the progressive detwinning through boundary migration.

We further study the size effects of the simulation box on phase transformations. The length of all three sides of the simulation cell is either reduced by one-half or doubled, corresponding to 1/8 and 8 times the previous volume, respectively. As shown in Figs. 7(e) and 7(f), the size effect is small on phase transition temperatures, indicating that the present MD predictions can well represent those of bulk NiTi. Indeed, the MD-predicted temperatures are only slightly lower (by 20 K) compared to experimental values.[56] On the other hand, a size effect is observed on the magnitude of W. Namely, at the end of stage II of cooling, W decreases with the increasing size of the simulation box, implying that W will reach its lower limit of zero in bulk NiTi. This trend is expected because the twin variants in a large system can better self-accommodate their respective shear distortion, thereby reducing the overall (averaged) shear deformation. But the quantification of the size limit giving $W \approx 0$ is not feasible yet, due to the computational limitation on the time scale of MD simulations of large atomic systems. On the other hand, W increases as the size of the simulation box decreases. This is understandable by noting the following limit. For the smallest simulation box with one unit cell, the formation of twinned microstructures is completely suppressed because of the geometrical constraint of the simulation cell, so that W has to stay at its upper limit of 1.

IV. SUMMARY AND CONCLUSION

Combining the crystallographic theory of twinned martensite with atomistic simulations, we study the nanoscale twins and martensitic phase transformations in NiTi with the multilattice structure. We explore the geometrical limits of nanotwins by showing the possible formation of a nontrivial mode of twinned martensites: different sublattices undergo different martensitic transformations. These twin structures are metastable and likely to be attainable in nanoscale compound twins, as hinted by the HRTEM images by Waitz *et al.*[26] Our molecular dynamics simulations predict the phase transformation temperatures, consistent with experimental measurements.[56] We find both the formation of twinned microstructures and associated overall shear deformation are sensitive to the size of the simulation system.

The present atomistic study focuses on the structural aspects of nanoscale compound twins. In view of the imprecision of empirical interatomic potential, verification via experiments and first principles calculations is needed to ascertain the conclusions. However, our results reveal the complexity of martensitic phase transformations at the sublattice level, and provide a structural basis for further atomistic study, as well as multiscale modeling of the NiTi phase transformations through bridging the crystallographic theory with atomistic and quantum mechanical calculations. Further, to fully reveal the physical origin of formation of nanotwins, the determination of the multilayer generalized gamma surface[29,57] is needed. This type of calculation has been performed for elemental metals,[57] but not NiTi with the multilattice structure. Finally, we note that the elemental metals (e.g., Cu) with nanotwins exhibited unusual properties, e.g., ultrahigh strength with retained ductility and high electrical conductivity,[58,59] the strongest twin size around 15 nm,[60,61] etc. Nanotwins in alloy and compound systems are more complicated, and possibly work in a very different way than normal metals. This work is a necessary step toward

understanding and exploiting the nanotwinned structure-property relationship in alloys and compounds with the complex multilattice structures.

ACKNOWLEDGMENTS

Support by NSF Grant Nos. CMMI-0825435 and C10-00243 is greatly acknowledged. The authors thank Olivier N. Pierron for helpful comments on this paper.

APPENDIX: SOLUTIONS OF TWINNING EQ. (5) FOR COMPOUND TWINS

We have used the crystallographic theory of twinned martensite[45] to facilitate the construction of initial twin structures. This theory only requires an input of the transformation matrix from the cubic parent phase to monoclinic martensitic phase. The twinning elements, including the twin plane normal n and twin shear vector m, can be predicted by solving the twinning equation of Eq. (5) in the text. This appendix provides the solution of twinning elements for compound twins. Their relaxed structures are discussed in the Sec. III. It should be noted that the general solutions provided by Hane and Shield[45] sometimes cannot be directly used in the atomistic simulation when periodic boundary conditions[48] are imposed to eliminate the free surface for studying bulk properties. In other words, it is necessary to construct the deformation gradient matrix such that the twin plane after martensitic transformation remains parallel to one side of the supercell for ensuring periodic twin structures in different supercells.

Consider a pair of symmetry-related transformation matrices

$$\mathbf{F}_I = \frac{1}{a_0}\begin{bmatrix} b/\sqrt{2} & 0 & 0 \\ 0 & c\sin\beta/\sqrt{2} & 0 \\ 0 & -c\cos\beta/\sqrt{2} & a \end{bmatrix},$$
$$\mathbf{F}_J = \frac{1}{a_0}\begin{bmatrix} b/\sqrt{2} & 0 & 0 \\ 0 & c\sin\beta/\sqrt{2} & 0 \\ 0 & c\cos\beta/\sqrt{2} & a \end{bmatrix}, \quad \text{(A1)}$$

We solve the twinning equation of Eq. (5) by following the procedure described by James and Hane (Ref. 3, Proposition 1, p. 202). Using the experimental values of lattice constant and monoclinic angle listed in Table I. we obtain two solutions: $\mathbf{n}^{\mathrm{I}} = [0,1,0]$, $\mathbf{m}^{\mathrm{I}} = [0,0,0.2566]$ and $\mathbf{n}^{\mathrm{II}} = [0,0,1]$, $\mathbf{m}^{\mathrm{II}} = [0,0.2252,-0.0268]$, which give the (010) and (001) compound twin, respectively. This pair of twins is conventionally called reciprocal or conjugate twins. Note that all the vectors are given in the $(\mathbf{i}',\mathbf{j}',\mathbf{k}')$ basis defined in Fig. 1.

Substitution of $\mathbf{n}^{\mathrm{I}}$ and $\mathbf{m}^{\mathrm{I}}$ into Eq. (5) yields $\mathbf{Q} = \mathbf{I}$. As discussed earlier, this result indicates that after the martensitic transformation of variants I and J, the orientation of the twin plane (010) is unchanged as illustrated in Fig. 8(a). This can be readily verified by noting that the twin plane normal after transformation, $\mathbf{n}^{\mathrm{I}}\mathbf{F}^{-1}$, is still along the $[0,1,0]$ direction.

In contrast, substitution of $\mathbf{n}^{\mathrm{II}}$ and $\mathbf{m}^{\mathrm{II}}$ into Eq. (5) yields $\mathbf{Q}$ unequal to the identity matrix. This is consistent with the fact that the orientation of the twin plane (001) is changed after martensitic transformation, as shown in Fig. 8(b). Indeed, the twin plane normal after transformation, $\mathbf{n}^{\mathrm{I}}\mathbf{F}^{-1}$, is in the $[0,0,1]$ direction. To ensure the periodicity of (001) compound twins in different supercells, we construct a pair of transformation matrices that are equivalent to those given by Eq. (A1), but keep the twin plane unrotated after martensitic transformation [see Fig. 8(c)],

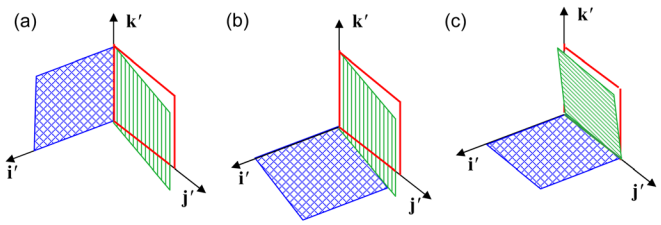

FIG. 8. (Color online) Illustration of shear transformation and the rotation of the mirror twin plane during the formation of (010) and (001) compound twins. (a) The (010) mirror twin plane (in blue) is unrotated after the shear transformation of the red rectangle to green parallelogram in the $(\mathbf{j}',\mathbf{k}')$ plane along the $\mathbf{k}'$ direction. (b) The (001) mirror twin plane (in blue) is rotated after the same shear transformation as (a). (c) The (001) mirror twin plane (in blue) is unrotated after the shear transformation of the red rectangle to green parallelogram in the $(\mathbf{j}',\mathbf{k}')$ plane along the $\mathbf{j}'$ direction.

$$\mathbf{F}_I^* = \frac{1}{a_0}\begin{bmatrix} b/\sqrt{2} & 0 & 0 \\ 0 & c/\sqrt{2} & -a\cos\beta \\ 0 & 0 & a\sin\beta \end{bmatrix},$$
$$\mathbf{F}_J^* = \frac{1}{a_0}\begin{bmatrix} b/\sqrt{2} & 0 & 0 \\ 0 & c/\sqrt{2} & a\cos\beta \\ 0 & 0 & a\sin\beta \end{bmatrix}. \quad \text{(A2)}$$

The above-presented matrices are constructed by noting that the martensitic transformation of the B2 to B19′ phase can be considered as an expansion or contraction along the edges of a tetragonal unit cell (see Fig. 1), followed by a simple shear to a monoclinic angle β. This simple shear can be achieved by rotating the $\mathbf{j}'$ axis about the i' axis, giving Eq. (A1) or equivalently by rotating $\mathbf{k}'$ about $\mathbf{i}'$, giving Eq. (A2). Solution of Eq. (1) with an input of Eq. (A2) gives compound twins of $\mathbf{n}^{\mathrm{I}} = [0,1,0]$, $\mathbf{m}^{\mathrm{I}} = [0,-0.0304,0.2550]$ and $\mathbf{n}^{\mathrm{II}} = [0,0,1]$, $\mathbf{m}^{\mathrm{II}} = [0,0.227,0]$. They are equivalent to the results from Eq. (A1), differing by a rotation.

Incidentally, Eq. (A2) can also be obtained by a more general procedure of starting from Eq. (A1) and then constructing a matrix that rotates the twin plane so that it is parallel to the side of the supercell, i.e., $\mathbf{F}_J^* = \mathbf{Q}^*\mathbf{F}_J$ and $\mathbf{F}_I^* = \mathbf{Q}^{*T}\mathbf{F}_J$, where

$$\mathbf{Q}^* = \begin{bmatrix} 1 & 0 & 0 \\ 0 & \sin\beta & \cos\beta \\ 0 & -\cos\beta & \sin\beta \end{bmatrix}. \quad \text{(A3)}$$

This "transformation and rotation" procedure is general, and can be applied to construct other types of twins in periodic supercells.

[1]K. Otsuka and C. Wayman, *Shape Memory Materials* (Cambridge University Press, Cambridge, UK, 1998).
[2]J. W. Christian and S. Mahajan, Progr. Mater. Sci. **39**, 1 (1995).

[3]R. D. James and K. F. Hane, Acta Mater. **48**, 197 (2000).
[4]K. Bhattacharya, *Microstructure of Martensite. Why It Forms and How It Gives Rise to the Shape-Memory Effect* (Oxford University Press, Oxford, UK, 2003).
[5]K. Otsuka and X. Ren, Progr. Mater. Sci. **50**, 511 (2005).
[6]T. Waitz, K. Tsuchiya, T. Antretter, and F. D. Fischer, MRS Bull. **34**, 814 (2009).
[7]T. Zhu and J. Li, Progr. Mater. Sci. **55**, 710 (2010).
[8]H. Sehitoglu, I. Karaman, R. Anderson, X. Zhang, K. Gall, H. J. Maier, and Y. Chumlyakov, Acta Mater. **48**, 3311 (2000).
[9]X. G. Ma and K. Komvopoulos, Appl. Phys. Lett. **83**, 3773 (2003).
[10]T. Waitz, V. Kazykhanov, and H. P. Karnthaler, Acta Mater. **52**, 137 (2004).
[11]A. J. M. Wood and T. W. Clyne, Acta Mater. **54**, 5607 (2006).
[12]C. P. Frick, T. W. Lang, K. Spark, and K. Gall, Acta Mater. **54**, 2223 (2006).
[13]C. P. Frick, S. Orso, and E. Arzt, Acta Mater. **55**, 3845 (2007).
[14]M. R. Daymond, M. L. Young, J. D. Almer, and D. C. Dunand, Acta Mater. **55**, 3929 (2007).
[15]A. Creuziger, L. J. Bartol, K. Gall, and W. C. Crone, J. Mech. Phys. Solids **56**, 2896 (2008).
[16]K. Gall, J. Tyber, G. Wilkesanders, S. W. Robertson, R. O. Ritchie, and H. J. Maier, Mater. Sci. Eng. A **486**, 389 (2008).
[17]J. S. Juan, M. L. No, and C. A. Schuh, Nat. Nanotechnol. **4**, 415 (2009).
[18]D. M. Norfleet, P. M. Sarosi, S. Manchiraju, M. F. X. Wagner, M. D. Uchic, P. M. Anderson, and M. J. Mills, Acta Mater. **57**, 3549 (2009).
[19]X. Huang and A. G. Ramirez, Appl. Phys. Lett. **95** (2009).
[20]J. Ye, R. K. Mishra, A. R. Pelton, and A. M. Minor, Acta Mater. **58**, 490 (2010).
[21]T. Simon, A. Kroger, C. Somsen, A. Dlouhy, and G. Eggeler, Acta Mater. **58**, 1850 (2010).
[22]M. S. Wechsler, D. S. Lieberman, and T. A. Read, Trans. Am. Inst. Min. Metall. Pet. Eng. **197**, 1503 (1953).
[23]J. M. Ball and R. D. James, Arch. Ration. Mech. Anal. **100**, 13 (1987).
[24]W. S. Lai and B. X. Liu, J. Phys.: Condens. Matter **12**, L53 (2000).
[25]X. Y. Huang, G. J. Ackland, and K. M. Rabe, Nat. Mater. **2**, 307 (2003).
[26]T. Waitz, D. Spisak, J. Hafner, and H. P. Karnthaler, Europhys. Lett. **71**, 98 (2005).
[27]X. Q. Wang, Phys. Rev. B **78**, 092103 (2008).
[28]N. Hatcher, O. Y. Kontsevoi, and A. J. Freeman, Phys. Rev. B **79**, 020202 (2009).
[29]N. Hatcher, O. Y. Kontsevoi, and A. J. Freeman, Phys. Rev. B **80**, 144203 (2009).
[30]S. Kibey, H. Sehitoglu, and D. D. Johnson, Acta Mater. **57**, 1624 (2009).
[31]K. G. Vishnu and A. Strachan, Acta Mater. **58**, 745 (2010).
[32]M. F. X. Wagner and W. Windl, Acta Mater. **56**, 6232 (2008).
[33]Q. P. Sun and K. C. Hwang, J. Mech. Phys. Solids **41**, 1 (1993).
[34]R. Abeyaratne and J. K. Knowles, J. Mech. Phys. Solids **41**, 541 (1993).
[35]S. Leclercq and C. Lexcellent, J. Mech. Phys. Solids **44**, 953 (1996).
[36]Z. K. Lu and G. J. Weng, J. Mech. Phys. Solids **45**, 1905 (1997).
[37]M. Huang and L. C. Brinson, J. Mech. Phys. Solids **46**, 1379 (1998).
[38]M. Cherkaoui, Q. P. Sun, and G. Q. Song, Int. J. Solids Struct. **37**, 1577 (2000).
[39]P. Thamburaja and L. Anand, J. Mech. Phys. Solids **49**, 709 (2001).
[40]T. J. Lim and D. L. McDowell, J. Mech. Phys. Solids **50**, 651 (2002).
[41]E. Patoor, D. C. Lagoudas, P. B. Entchev, L. C. Brinson, and X. J. Gao, Mech. Mater. **38**, 391 (2006).
[42]T. Waitz, T. Antretter, F. D. Fischer, N. K. Simha, and H. P. Karnthaler, J. Mech. Phys. Solids **55**, 419 (2007).
[43]A. Sengupta and P. Papadopoulos, Comput. Methods Appl. Mech. Eng. **198**, 3214 (2009).
[44]C. H. Lei, L. J. Li, Y. C. Shu, and J. Y. Li, Appl. Phys. Lett. **96**, 141910 (2010).
[45]K. F. Hane and T. W. Shield, Acta Mater. **47**, 2603 (1999).
[46]X. D. Ding, T. Suzuki, X. B. Ren, J. Sun, and K. Otsuka, Phys. Rev. B **74**, 104111 (2006).
[47]M. W. Finnis and J. E. Sinclair, Philos. Mag. A **50**, 45 (1984).
[48]M. Parrinello and A. Rahman, J. Appl. Phys. **52**, 7182 (1981).
[49]S. Huang, S. L. Zhang, T. Belytschko, S. S. Terdalkar, and T. Zhu, J. Mech. Phys. Solids **57**, 840 (2009).
[50]K. M. Knowles and D. A. Smith, Acta Metall. **29**, 101 (1981).
[51]T. M. Brill, S. Mittelbach, W. Assmus, M. Mullner, and B. Luthi, J. Phys.: Condens. Matter **3**, 9621 (1991).
[52]O. Mercier, K. N. Melton, G. Gremaud, and J. Hagi, J. Appl. Phys. **51**, 1833 (1980).
[53]R. S. Elliott, J. A. Shaw, and N. Triantafyllidis, J. Mech. Phys. Solids **54**, 193 (2006).
[54]M. Dobson, R. S. Elliott, M. Luskin, and E. B. Tadmor, J. Comput.-Aided Mater. Design **14**, 219 (2007).
[55]J. R. Morris, Y. Ye, M. Krcmar, and C. L. Fu, in *Advanced Intermetallic-Based Alloys, Materials Research Society Symposia Proceedings No. 980*, edited by J. Wiezorek, C. L. Fu, M. Takeyama, D. Morris, and H. Clemens (Materials Research Society, Warrendale, PA, 2007), p. II06.
[56]S. Miyazaki and K. Otsuka, Metall. Trans. A **17**, 53 (1986).
[57]S. Ogata, J. Li, and S. Yip, Phys. Rev. B **71**, 224102 (2005).
[58]L. Lu, Y. F. Shen, X. H. Chen, L. H. Qian, and K. Lu, Science **304**, 422 (2004).
[59]T. Zhu, J. Li, A. Samanta, H. G. Kim, and S. Suresh, Proc. Natl. Acad. Sci. U.S.A. **104**, 3031 (2007).
[60]L. Lu, X. Chen, X. Huang, and K. Lu, Science **323**, 607 (2009).
[61]X. Y. Li, Y. J. Wei, L. Lu, K. Lu, and H. J. Gao, Nature (London) **464**, 877 (2010).